Science of the Total Environment 724 (2020) 138167

Contents lists available at ScienceDirect

Science of the Total Environment

journal homepage: www.elsevier.com/locate/scitotenv

Improved degradation of etodolac in the presence of core-shell $ZnFe_2O_4/SiO_2/TiO_2$ magnetic photocatalyst

Eryka Mrotek [a], Szymon Dudziak [a], Izabela Malinowska [a], Daniel Pelczarski [c], Zuzanna Ryżyńska [b], Anna Zielińska-Jurek [a,*]

[a] Department of Process Engineering and Chemical Technology, Gdansk University of Technology, Narutowicza 11/12, 80-233 Gdansk, Poland
[b] Department of Solid State Physics, Gdansk University of Technology, Poland
[c] Department of Physics of Electronic Phenomena, Gdansk University of Technology, Poland

HIGHLIGHTS

- Degradation of etodolac in the presence of $ZnFe_2O_4/SiO_2/TiO_2$ was significantly improved under UV-Vis
- After 20 min of irradiation in the presence of $ZnFe_2O_4/SiO_2/TiO_2$ almost 100% of etodolac was degraded
- The reactive oxygen species $\bullet O_2^-$ and h+ plays an important role in the photodegradation of etodolac
- The obtained p-type TiO_2-based photocatalyst coupled with zinc ferrite in a core-shell structure improves the separation and recovery of nanosized TiO_2
- The Mott-Schottky analysis confirmed that the magnetic photocatalyst can efficiently oxidize H_2O to produce superoxide radicals

GRAPHICAL ABSTRACT

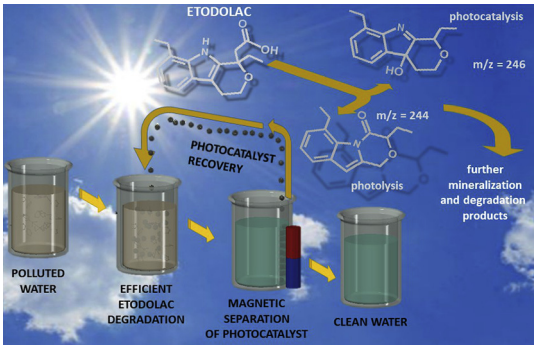

ARTICLE INFO

Article history:
Received 19 January 2020
Received in revised form 6 March 2020
Accepted 22 March 2020
Available online 28 March 2020

Editor: Yifeng Zhang

Keywords:
Photocatalytic degradation
Etodolac
Indoles
Magnetic photocatalyst
Pharmaceutical removal

ABSTRACT

In the present study, susceptibility to photocatalytic degradation of etodolac, 1,8-diethyl-1,3,4,9 – tetrahydro pyran - [3,4-b] indole-1-acetic acid, which is a non-steroidal anti-inflammatory drug frequently detected in an aqueous environment, was for the first time investigated. The obtained p-type TiO_2-based photocatalyst coupled with zinc ferrite nanoparticles in a core-shell structure improves the separation and recovery of nanosized TiO_2 photocatalyst. The characterization of $ZnFe_2O_4/SiO_2/TiO_2$, including XRD, XPS, TEM, BET, DR/UV–Vis, impedance spectroscopy and photocatalytic analysis, showed that magnetic photocatalyst containing anatase phase revealed markedly improved etodolac decomposition and mineralization measured as TOC removal compared to photolysis reaction. The effect of irradiation and pH range on photocatalytic decomposition of etodolac was studied. The most efficient degradation of etodolac was observed under simulated solar light for a core-shell $ZnFe_2O_4/SiO_2/TiO_2$ magnetic photocatalyst at pH above 4 (pKa = 4.7) and below 7. The irradiation of etodolac solution in a broader light range revealed a synergetic effect on its photodegradation performance. After only 20 min of degradation, about 100% of etodolac was degraded. Based on the photocatalytic analysis in the presence of scavengers and HPLC analysis, the transformation intermediates and possible photodegradation pathways of etodolac were studied. It was found that $\cdot O_2^-$ attack on C2-C3 bond inside pyrrole ring results mostly in the hydroxylation

* Corresponding author.
E-mail address: annjurek@pg.edu.pl (A. Zielińska-Jurek).

https://doi.org/10.1016/j.scitotenv.2020.138167
0048-9697/

of the molecule, which next undergoes -CH_2COOH detachment to give 1,9-diethyl-3,4-dihydro-pyrano[3,4-*b*] indol-4a-ol. The obtained compound should further undergo subsequent hydropyran and pyrrole ring breaking to give a family of benzene derivatives.

1. Introduction

Etodolac, 1,8-diethyl-1,3,4,9–tetrahydro pyran-[3,4-b] indole-1-acetic acid is used worldwide as an anti-inflammatory, analgesic and antipyretic drug to treat rheumatoid arthritis, chronic soft tissue inflammation (vessels, tendons), nerve inflammation and osteoporosis (Gadade et al., 2017; Brocks and Jamali, 1994). This pharmaceutical agent is metabolized in the liver. Although only 1% of etodolac is excreted unchanged from the human body by the kidneys in the urine and 16% in the feces, etodolac is frequently detected in the aqueous environment, e.g., rivers, lakes or surface waters (Hoshina et al., 2011; Temussi et al., 2011; Saxena et al., 2016). In 2011, etodolac (ETD) was detected in river water samples in Hyogo in Japan at a concentration of 0.3 $ng \cdot dm^{-3}$ (Hoshina et al., 2011). In 2019, Guzel et al. reported its presence in the concentration of 47.35 $ng \cdot dm^{-3}$ in the Ceyhan River in south Turkey (Guzela et al., 2019). ETD has a negative effect on aquatic organisms such as alga, daphnid, and fish. Causing disorders in normal development or impairing already formed living organisms (Watanabe et al., 2016). Passananti et al. investigated the parent compound ETD and its derivatives for toxicity to aquatic organisms such as rotifers, algae, and crustaceans (Passananti et al., 2015). It was reported that the concentration of 25 $mg \cdot dm^{-3}$ for crustaceans and 10 $mg \cdot dm^{-3}$ in long-term exposure to algae does not lead to mortality but disturbs and even inhibits the reproduction of the aquatic individuals. The adequate concentration of etodolac in living organisms depends on the level of education of the living organism. However, what is particularly important, etodolac and its' derivatives, are susceptible to bioaccumulation (Howard and Muir, 2011).

The bicyclic indole system present in the structure of etodolac is found in many biological molecules (Passananti et al., 2015). Therefore, etodolac is resistant to biological degradation but undergoes photolysis. Saxena et al. studied the degradation of etodolac in acid and base hydrolysis, hydrogen peroxide oxidation, thermal degradation, and photolysis (Saxena et al., 2016) and observed complete degradation after 8 h in acidic conditions (5 M HCl) and a temperature of 60 °C. Passananti et al. focused on the photochemical properties of etodolac under UV-B, UV-A, and direct exposure to sunlight. Direct photolysis involves the transformation of xenobiotic molecules resulting from the direct absorption of radiation. The efficient degradation was observed by photolysis under UV-B irradiation, while negligible degradation of etodolac occurred using UV-A and solar radiation (Passananti et al., 2015). Moreover, the photochemical study proved the oxygen involvement in etodolac transformation mainly by oxygen attack to the C2–C3 bond of the pyrrolic ring (Passananti et al., 2015). In this regard, advanced oxidation processes (AOPs), where nonselective free radical species chemically oxidize pollutants, occurred to be a promising method for degradation of etodolac in the aqueous phase. Free radical species produced in-situ in AOP processes, e.g., hydroxyl radical (HO•), superoxide anion radical ($•O_2^-$, hydroperoxyl radical ($HO_2•$), alkoxyl radical (RO•) or single oxygen ($^1O_2$) can initiate AOPs to degrade active pharmaceutical ingredients (APIs) to simple and non-toxic molecules. Among the advanced oxidation processes, heterogeneous photocatalytic oxidation has resulted in the efficient degradation of different pharmaceuticals and their removal from water and wastewater (Kanakaraju et al., 2018). As far as we know, the photocatalytic decomposition of etodolac has not been studied yet.

Titanium(IV) oxide is the most commonly used photocatalyst for environmental applications due to its non-toxic nature, chemical stability, insolubility in the medium, low cost, and high photocatalytic activity (Ohtani, 2010). However, in a technological process, there are several problems with cyclic utilization of the powdered nano-TiO_2 particles suspended in the treated water. Owing to nanometric particle size, the TiO_2 could be recovered from the treated wastewater mostly by ultrafiltration (Lee et al., 2001) Another possibility is the immobilization of semiconductors' particles on a solid substrate, which can result in a significant decrease in a specific surface area and thus decrease the photocatalytic activity. Moreover, the TiO_2 layer is often unstable and undergoes abrasion during the photodegradation reaction (Folli et al., 2010).

Recently, magnetic photocatalysts, where semiconductor nanoparticles, usually TiO_2 and ZnO, are deposited on the surface of ferrite (Fe_3O_4, Fe_2O_4, $CoFe_2O_4$, $ZnFe_2O_4$, $BaFe_{12}O_{19}$) allowing easy separation of a photocatalyst from the system after the purification process, are considered as the most perspective (Zielińska-Jurek et al., 2017a; Mishra et al., 2019). Mostly, the described in literature activity of magnetic nanocomposites' is focused on the organic dyes' degradation (Meng et al., 2018). Previously, Zielińska-Jurek et al. studied the structural, photocatalytic, and magnetic properties of Fe_3O_4@ SiO_2/TiO_2 nanocomposites in organic compounds (pyridine, phenol, 4-heptanone) degradation as well as their mineralization in the flow back fluid after hydraulic fracturing process (Zielińska-Jurek et al., 2017b). Abdel-Wahab et al. (Abdel-Wahab et al., 2017) focused on the degradation of paracetamol over magnetic flower-like TiO_2/Fe_2O_3 core-shell nanostructures. Its complete mineralization was observed after 90 min of irradiation.

Similarly, the Fe_3O_4/TiO_2 core structure - Ni/Co doping - coating nanocomposites used in Amlodipine drug photodegradation allowed for pharmaceutical compound decomposition after 90 min of exposure in the UV–Vis range (Teimouri et al., 2019). However, to our knowledge, data on the photocatalytic degradation of etodolac using TiO_2-based magnetic photocatalyst have not been reported in the literature.

In this regard, for the first time, the present work reports about photocatalytic degradation of etodolac in the presence of $ZnFe_2O_4/SiO_2/TiO_2$ magnetic photocatalyst. $ZnFe_2O_4$-based hybrid photocatalysts possess magnetic properties that allow effective separation in the external magnetic field after degradation reaction (Lee et al., 2001). Zinc ferrite core was coated with silica layer to (i) increase the surface area of the composite material allowing better adsorption of degraded pollutants and (ii) prevent photodissolution of iron as well as phase transformation of $ZnFe_2O_4$ during the photocatalytic reaction. The external photocatalytic layer based on TiO_2 is directly responsible for the oxidation of etodolac.

Etodolac direct photolytic decomposition and its photocatalytic degradation in the presence of magnetic photocatalyst under UV and Vis light at different pH values were studied. The reaction kinetics were interpreted with the molecular structures of the chemicals and the characteristics of the UV–Vis wavelengths. The reusability of $ZnFe_2O_4/SiO_2/TiO_2$ magnetic photocatalyst was studied in the six subsequent cycles of etodolac degradation. Based on the obtained results, a possible mechanism for the photocatalytic decomposition of etodolac was proposed.

2. Experimental

2.1. Preparation of $ZnFe_2O_4/SiO_2/TiO_2$ magnetic photocatalysts

Titanium butoxide (pure p.a.) was purchased from Aldrich and used as a titanium(IV) oxide source. Zinc chloride, iron sulfate heptahydrate, sodium hydroxide were purchased from Aldrich. Firstly, to obtain zinc ferrite particles, $FeSO_4{\cdot}7H_2O$ and $ZnCl_2$ were dissolved in stoichiometric 2:1 (Fe: Zn) molar ratio in distilled water under stirring (500 rpm) for 30 min. Afterward, the metals were precipitated from the homogenous solution by adding 5 M NaOH at room temperature until a pH was 12. The reaction mixture was hydrothermally treated in an autoclave at 200 °C for 5 h. Subsequently, the solid product of the reaction was magnetically separated and purified with deionized water several times. The final product was dried at 100 °C to dry mass.

Furthermore, the magnetic particles were re-dispersed in ethanol, and tetraethyl orthosilicate (TEOS) was added to the suspension to obtain a silica layer. Afterward, ammonia water was added. The molar ratio of TEOS to $ZnFe_2O_4$ and NH_4OH to TEOS was equal to 8:1 and 16:1, respectively. The $ZnFe_2O_4/SiO_2$ particles were magnetically separated, washed with ethanol and deionized water, and dried at 60 °C to dry mass.

Following that, $ZnFe_2O_4/SiO_2$ particles were dispersed in isopropanol ethanolic solution, and titanium(IV) butoxide (TBT) was added. The rate of TBT addition was kept at 0.5 $cm^3{\cdot}min^{-1}$. Finally, the obtained gel was treated in a Teflon-lined autoclave at 200 °C for 24 h, resulting in the preparation of the $ZnFe_2O_4/SiO_2/TiO_2$_I photocatalyst. The obtained composite material was calcined at 400 °C (sample $ZnFe_2O_4/SiO_2/TiO_2$_400) as well as at 650 °C for 1 h (sample $ZnFe_2O_4/SiO_2/TiO_2$_650_I).

Additional samples of magnetic photocatalysts $ZnFe_2O_4/SiO_2/TiO_2$_II and $ZnFe_2O_4/SiO_2/TiO_2$_650_II were prepared by adding cationic surfactant (CTAB) into the solution during the preparation of magnetic core - photocatalytic layer composite at alkaline conditions (pH of 8). In this regard, $ZnFe_2O_4/SiO_2$ particles were dispersed in isopropanol, and CTAB ethanolic solution added dropwise into a mixture, with the molar ratio of TiO_2 to CTAB equaled to 1:1. Then, titanium(IV) butoxide (TBT) was added with a rate kept at 0.5 $cm^3{\cdot}min^{-1}$. Finally, the suspension was treated in a Teflon-lined autoclave at 200 °C for 24 h resulting in the preparation of the core-interlayer-shell $ZnFe_2O_4/SiO_2/TiO_2$ photocatalysts. The obtained product was separated and purified with deionized water several times to remove the surfactant before drying at 60 °C (sample $ZnFe_2O_4/SiO_2/TiO_2$_II) and calcination at 650 °C for 1 h (sample $ZnFe_2O_4/SiO_2/TiO_2$_650_II).

2.2. Characterization of $ZnFe_2O_4/SiO_2/TiO_2$ magnetic photocatalysts

X-ray powder diffraction (XRD) analysis was performed using Rigaku MiniFlex 600 X-ray diffractometer (Rigaku Corporation, Tokyo, Japan). The patterns were obtained in step-scanning mode ($\Delta 2\theta = 0.01°$) in the range from 20° to 80° 2θ. The crystalline and amorphous phase content was analyzed using an internal standard (NiO, Aldrich, Germany).

The magnetic properties of coated ferrite nanocomposites were investigated using the Physical Properties Measurements System (Quantum Design, San Diego, CA, USA) at the temperature of 293 K and in the range of 0–3 T. The diffuse reflectance (DR) spectra were analyzed using a Thermo Scientific Evolution 220 spectrophotometer (Waltham, MA, USA) with an integrating. Nitrogen adsorption-desorption isotherms were analyzed using the Micromeritics Gemini V instrument. Surface charges (zeta potential) and particle size were measured using Nano-ZS Zetasizer dynamic light scattering detector (Malvern Instruments, UK) equipped with a 4.0 mW internal laser. The fluorescence spectra of the $ZnFe_2O_4/SiO_2/TiO_2$ photocatalysts were measured using a fluorescence spectrophotometer (Perkin Elmer LS55). The morphology of the prepared photocatalysts was determined by high-resolution transmission electron microscopic analysis (HR-TEM) using an electron microscope (TEM, FEI Europe, Tencai F20 X-Twin. For TEM analysis, $ZnFe_2O_4/SiO_2/TiO_2$ particles were dispersed in ethanol and placed in an ultrasound bath for 1 min. Subsequently, a few drops of suspension were deposited on Lacey Carbon microgrid. XPS spectrophotometer (Escalab 250Xi, Thermofisher Scientific) was used to determine the surface composition of the photocatalytic material. Electrochemical impedance spectroscopy (EIS) was studied using the potentiostat-galvanostat (AutoLab PGStat302N system, Utrecht, The Netherlands) under GPES/FRA software control. Electrochemical impedance spectroscopy (EIS) analysis was perfomed in a three-electrode cell in 0,2 K_2SO_4 solution using the potentiostat-galvanostat (AutoLab PGStat302N system, Utrecht, The Netherlands) under GPS/FRA software control. As a reference electrode Ag/AgCl in 0.1 M KCl was applied, while platinum mesh was used as a counter electrode. The spectra were run at the frequency range from 20 kHz to 0,1 Hz with a 50 mV amplitude of the alternating current.

2.3. Photocatalytic degradation of etodolac

The photocatalytic activity was studied as examining the rate of etodolac degradation. In this regard, 0.05 g of the photocatalysts' particles was added to a quartz reactor containing 25 cm^3 of etodolac (ETD) solution with an initial concentration of 15 $mg{\cdot}dm^{-3}$. The suspension was stirred and aerated. During the photocatalytic process, the reactor was irradiated using a 300 W Xenon lamp (Photonics Hamamatsu, Japan), as ultraviolet-visible (UV–Vis) light source. To assess the degradation in visible light, a GG filter that transmitted light wavelength >400 nm was used. During the photocatalytic process, samples of 1 cm^3 of the suspension were collected at regular time intervals. The pharmaceuticals' degradation rate was measured as a pharmaceutical concentration decrease using HPLC chromatograph Shimadzu LC-6A (Kyoto, Japan) combined with (SPD-M20A) photodiode array detector. During the measurements, a mobile phase consisting of 1:1 (v/v) acetonitrile and 0,1 M KH_2PO_4 solution mixture was used at 1 $cm^3{\cdot}min^{-1}$ flow, together with Phenomenex Gemini 5 μm C18; 150 × 4,6 mm column working at 45 °C. Etodolac identification and further quantification were based on a standard compound and performed external calibration for a characteristic 273 nm signal.

3. Results

3.1. Characterization of $ZnFe_2O_4/SiO_2/TiO_2$ photocatalysts

The physicochemical characteristics of the magnetic photocatalysts e.g., crystallite sizes, indirect band gap values, BET surface areas are given in Table 1.

The composition of the crystalline phase was examined by XRD analysis for both as-obtained ferrite and its further modifications, and the results are shown in Fig. 1. Formation of pure $ZnFe_2O_4$ was confirmed by the presence of the signals at 2θ of 18.16°; 29.8°; 35.2°; 42.8°; 53.1°; 56.5° and 62.1°, which corresponds to JCPDS card No. 82-1042. The broad reflections indicated the formation of fine ferrite crystallites with a size of about 10 nm (see in Table 1). The deposition of both SiO_2 and TiO_2 layers resulted in a visible weakening of $ZnFe_2O_4$ signals. However, most of the composite material remained amorphous (~80%) before calcination.

Calcination of $ZnFe_2O_4/SiO_2/TiO_2$_I sample at 400 °C resulted in both the appearance of more intense TiO_2 signals and crystallites growth to approximately 11.5 nm. The reflections at 2θ of 25.3°; 36.9°; 37.7°; 48.0°; 53.9°; 62.7° corresponded to anatase crystal planes (101), (103), (004), (200), (105), (204), respectively (JCPDS card No. 89-4203). The sample $ZnFe_2O_4/SiO_2/TiO_2$_400 composed of anatase (39%) and amorphous phase of TiO_2 and SiO_2 (48.5%), without rutile. The formation of the rutile phase occurs above 600 °C (Mansour, 2019; Ohtani et al., 1997). In this regard, to enhance charge carrier separation, the

Table 1
Characteristics of the obtained ferrite particles and magnetic composite materials.

Sample label	TiO_2 Source	Preparation condition		Crystallite size [nm]		Phase content [%]				BET Surface Area [m^2/g]	V_{por} [cm^2/g]	E_g [eV]
		Surfactant	Calcination temperature [° C]	Anatase	Zinc ferrite	Anatase	Rutile	Zinc ferrite	Amorphous phase			
$ZnFe_2O_4$	–	–	–	–	10	–	–	58.5	41.5	25	0.012	1.68
$ZnFe_2O_4/SiO_2$	–	–	–	–	10	–	–	34	66	62	0.030	1.88
$ZnFe_2O_4/SiO_2/TiO_2$_I	TBT	–	–	2	10	5	–	15	80	187	0.092	3.33
$ZnFe_2O_4/SiO_2/TiO_2$_II	TBT	CTAB	–	2	10.5	5	–	15	80	106	0.051	2.98
$ZnFe_2O_4/SiO_2/TiO_2$_400	TBT	–	400	11.5	11	39	–	12.5	48.5	75	0.037	3.13
$ZnFe_2O_4/SiO_2/TiO_2$_650_I	TBT	–	650	20	12	46	3	19	32	50	0.025	3.18
$ZnFe_2O_4/SiO_2/TiO_2$_650_II	TBT	CTAB	650	31.5	12	47	4.5	8.5	40	18	0.009	3.25

obtained magnetic photocatalyst particles were also calcined at 650 °C. Previously, for the most photocatalytic active TiO_2 powder (P25, Evonik), Ohno et al. proofed that the fairly high photoreactivity of this material results from the creation of heterojunction between anatase-rutile particles (Ohno et al., 2001). The fine rutile crystallites facilitate the e^- transport to anatase trapping sites and thus forming photocatalytic hot spots at the rutile-anatase interface (Gambarotti et al., 2012). The diffraction peaks at 2θ of 35.2°; 53.9°; 56.7°; 62.2° demonstrates the possible presence of rutile clusters (JCPDS, No. 76-1940). For the samples $ZnFe_2O_4/SiO_2/TiO_2$_650_I and $ZnFe_2O_4/SiO_2/TiO_2$_650_II containing anatase phase (~46-47%) with a small amount of rutile (3–4.5%), higher crystallinity (60–68%) than for $ZnFe_2O_4/SiO_2/TiO_2$_400 (~51.5%) was observed.

Moreover, no crystallites growth of $ZnFe_2O_4$ was observed, suggesting that formed ferrite particles should be tightly covered with SiO_2/TiO_2 layer, which prevents it from further growth (approx. crystallites size of 10 nm, and 11 nm for the as-obtained $ZnFe_2O_4$ and after 400 °C calcination, respectively). Finally, no crystallization of silica was observed, suggesting that SiO_2 remains an amorphous layer. Crystallization of SiO_2 is kinetically difficult and starting above 600 °C (Tomita and Kawano, 1993).

The specific surface area of bare zinc ferrite was 25 $m^2 \cdot g^{-1}$ and increased after coating with SiO_2 layer to 62 $m^2 \cdot g^{-1}$. Further, for $ZnFe_2O_4/SiO_2/TiO_2$_I and $ZnFe_2O_4/SiO_2/TiO_2$_II samples coated with TiO_2 layer, the specific surface area increased to 187 $m^2 \cdot g^{-1}$ and 106 $m^2 \cdot g^{-1}$, respectively, and finally decreased for samples calcined at 400 °C and 650 °C. The BET area of $ZnFe_2O_4/SiO_2/TiO_2$_400 and $ZnFe_2O_4/SiO_2/TiO_2$_650_I decreased from 75 $m^2 \cdot g^{-1}$ to 50 $m^2 \cdot g^{-1}$ with increasing calcination temperature from 400 °C to 650 °C and anatase crystallite size increased from 11.5 nm to 20 nm, respectively. Increased crystallites size observed for the annealed samples results from the crystallization of the TiO_2 structure from amorphous precursor as well as from minimalization of the surface energy as the grain/crystallites boundary is reduced through their growth. The amorphous phase is metastable, and the surface formation is always accompanied by the energy barrier, which should tend to minimize both factors (Porter et al., 1995; Zhang et al., 2000). At higher temperatures, the mobility/diffusion of atoms inside solids is facilitated by the temperature. In this regard, the observed behavior for the obtained samples is consistent with the basic mechanisms of crystallization. For $ZnFe_2O_4/SiO_2/TiO_2$_650_II core-shell photocatalyst obtained in the presence of cationic surfactant, which acts as a binder of $ZnFe_2O_4/SiO_2$ and TiO_2 layer, further reduction in specific surface area to 18 $m^2 \cdot g^{-1}$ and increase of anatase crystallite size to 30 nm was noticed. Regarding the literature, the use in this study excess of cationic surfactant (2-times higher than CMC value) may lead to the formation of the second layer of surfactant and cylindrical micelles containing several core-shell nanoparticles in crystalline structure (Liu et al., 2013).

The TEM microscopy analysis, shown in Fig. 2, confirmed the formation of the core-shell structure of $ZnFe_2O_4/SiO_2/TiO_2$ nanoparticles with

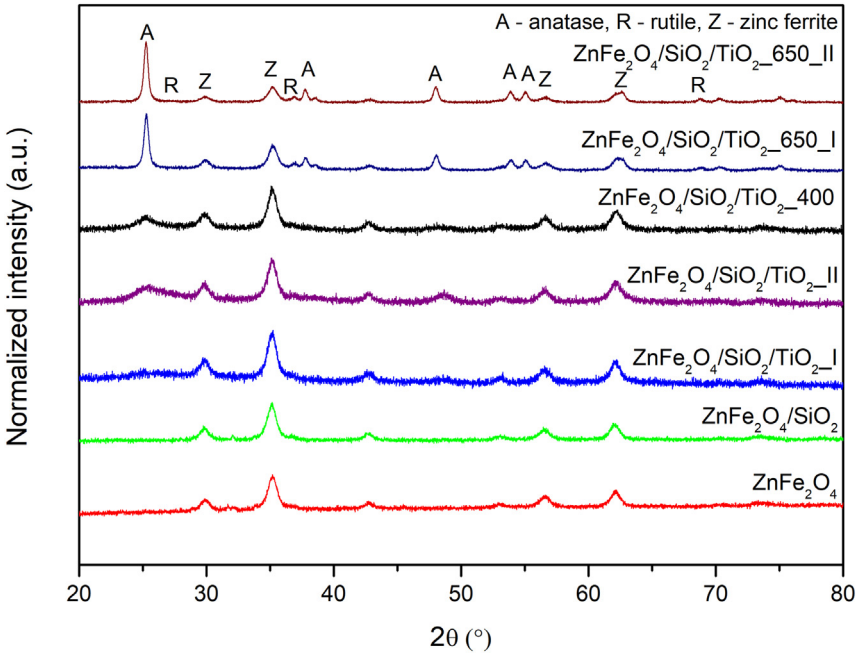

Fig. 1. XRD diffraction patterns of the as-prepared $ZnFe_2O_4$, $ZnFe_2O_4/SiO_2$, and $ZnFe_2O_4/SiO_2/TiO_2$ magnetic photocatalysts calcined in 400 °C and 650 °C.

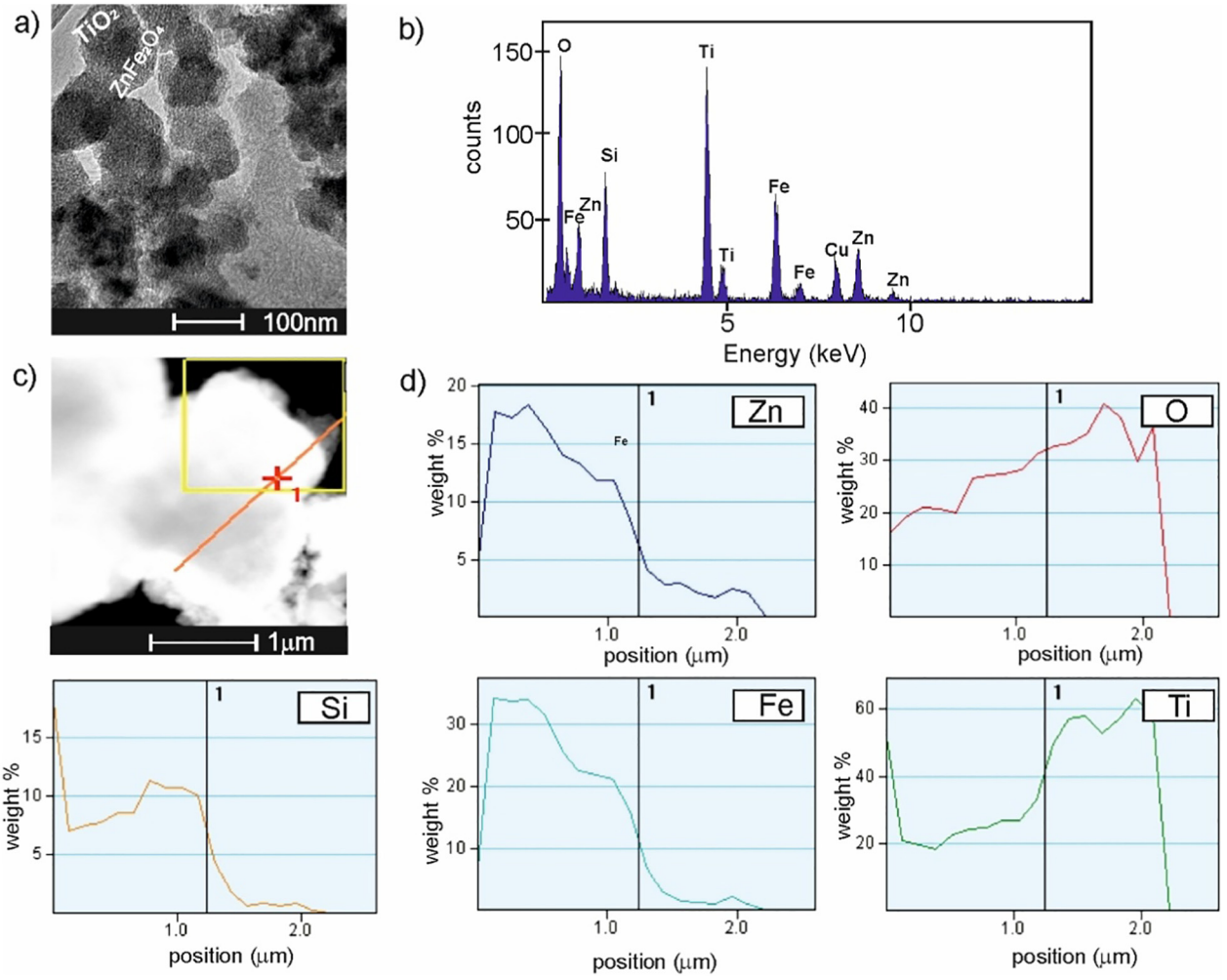

Fig. 2. Morphology (TEM images) (a), EDS and EDS-line measurements (b-c) of $ZnFe_2O_4/SiO_2/TiO_2$_650_II photocatalyst.

the total composite particle size of about 50–60 nm (Fig. 2a). The average particle size of the samples is larger than nanocrystals size calculated based on XRD measurements, which confirmed that the zinc ferrite core (~10 nm) is coated with a TiO_2 shell (~30 nm). The particles were spherical and uniformly distributed, and agglomeration of grains was caused by the magnetic attractions. Additional TEM images of the prepared magnetic photocatalyst are shown in the Supplementary materials (Fig. S1). The Energy Dispersive Spectroscopy (EDS) revealed the presence of Zn, Fe, Si, O, and Ti in the structure of the as-prepared photocatalytic material (Fig. 2b). Moreover, the EDS line scanning profiles (Fig. 2c–d) across the particle also showed that it consisting of zinc ferrite core and titania shell. The signals for Zn and Fe occurred in the same area inside the structure, while the signals for Si, O, and Ti outside the structure of the magnetic particle.

It can be concluded from EDX analysis that all basic elements of $ZnFe_2O_4/SiO_2/TiO_2$ exist in the prepared composite nanomaterial, as confirmed by XRD characterization, as well.

The survey of XPS spectra of $ZnFe_2O_4/SiO_2/TiO_2$_650_II photocatalyst recorded in the binding energy (BE) range of 0 to 1300 eV is presented in Fig. S2 in the Supporting materials. Several peaks associated with Ti, O, and a trace amount of Si, Zn, Fe are detected, as well as a signal identified with the C 1s peak. Fig. S2b shows that binding energy of 458.5 eV corresponds to the peak of Ti $2p_{3/2}$, whereas binding energy of 464.3 eV is associated with Ti $2p_{1/2}$. The Ti 2p binding energies indicate the incorporation of Ti into the lattice of TiO_2 as Ti^{4+}. Moreover, the Auger signals assigned to the Ti LMV transition were observed. As presented in Table S1 in the Supplementary materials, the titanium content was about 27 at.%. Exhibited in Fig. S2c are the O 1s components with the binding energies at 529.7 eV, 531.8 eV, and 532.9 eV, which are associated with different types of oxygen bonds. Two of the most intense peaks corresponded to lattice oxygen (Ti—O groups) and oxygen in hydroxyl groups (Ti–OH), respectively. The peak at about 103 eV, shown in Fig. S2d, could be assigned to Si–O-Si from the O 1s spectrum. The oxygen content was 49.7 at.%. The iron content was on the verge of noise

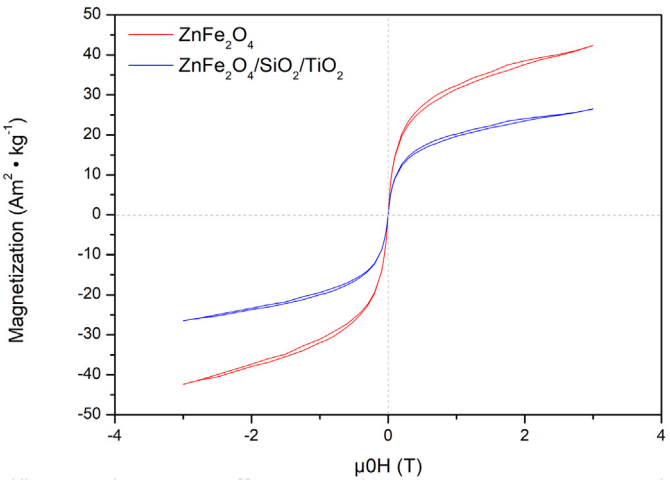

Fig. 3. Magnetic hysteresis loop of $ZnFe_2O_4$ and $ZnFe_2O_4/SiO_2/TiO_2$ photocatalyst.

detection (see in Fig. S2e), while the Zn $2p_{3/2}$ and Zn $2p_{1/2}$ components characteristic of a low amount of Zn^{2+} are located at 1021.2 eV and 1044.3 eV, respectively. The zinc content was 1.4 at.%. The origin of carbon presents (~13.9 at.%) is mainly attributed to atmospheric contaminants.

As shown in Fig. 3, as-obtained $ZnFe_2O_4$ ferrite particles exhibited strong ferrimagnetic properties with a saturation magnetization (*Ms*) of 40 emu·g^{-1} and can exhibit superparamagnetic behavior due to small coercivity (*Hc*) and remanent magnetization (*Mr*) values.

The obtained results are consistent with the reported for $ZnFe_2O_4$, revealing it as a soft ferromagnetic material with an extensive range of possible magnetization values (Yao et al., 2007). For an ideal magnetic particle, the *Ms* value should decrease together with the particle size due to the development of the surface area and possible defects, leading to the magnetic moments' misalignment. It was shown in detail far compounds like magnetite Fe_3O_4 (Lee et al., 2015; Mascolo et al., 2013). However, $ZnFe_2O_4$ behaves differently due to the preference to form a normal spinel structure in its bulk form, which was found to be antiferromagnetic (Yao et al., 2007; Lee et al., 2015; Mascolo et al., 2013; Mozaffari et al., 2010). Because of this, visible magnetic properties of zinc ferrite are mostly observed for its nanoparticles, for which cation distribution is usually at least partially inverted. The final magnetization of the $ZnFe_2O_4$, therefore, depends on both particle size and specific cation distribution, which was found to depend on particle shape, size, and specific preparation conditions e.g., pH (Mozaffari et al., 2010; Kurian and Mathew, 2018; Shanmugavani et al., 2014). After the formation of both SiO_2 and TiO_2 layers, the magnetization of the composite decreased to 25 emu·g^{-1}, as shown in Fig. 3 for $ZnFe_2O_4/SiO_2/TiO_2$ photocatalyst. It was expected since $ZnFe_2O_4$ make up only a small fraction of the final material. As revealed by the XRD and XPS analysis, TiO_2 and SiO_2 are the predominant in both $ZnFe_2O_4/SiO_2/TiO_2$_650 samples, and therefore the magnetization decrease should be proportional to their content.

The DR/UV–Vis spectra were measured to study the optical absorption properties of the magnetic photocatalysts. As shown in Fig. 4, all samples absorb UV light due to the sp-d interaction between valence band electrons of O and d electrons of Ti or Zn/Fe atoms in TiO_2 and $ZnFe_2O_4$ structures, respectively. The absorption properties decreased after the coating of $ZnFe_2O_4$ with SiO_2, indicating that the SiO_2 layer remarkably influenced the UV–Vis absorption ability of zinc ferrite particles, protecting them from photodissociation during the photocatalytic reaction. The light absorption edge in the ultraviolet region for nanocomposites was close to that of the pure titania particles. For all the $ZnFe_2O_4/SiO_2/TiO_2$ composites, the absorption was markedly red-shifted after the coating of $ZnFe_2O_4$ ferrite with SiO_2 and TiO_2 layer. Obtained spectra were transformed into the Kubelka-Munk function, and the Tauc transformation was used to determine the band gap energy. As expected, the $ZnFe_2O_4$ ferrite sample exhibited low band gap energy of 1.68 eV, and it widened after coating with silica to 1.88 eV, see in Table 1. According to literature, the band gap of pure TiO_2 particles depends on the polymorphs and is reported at ~3.0 eV for rutile and 3.2–3.3 eV for anatase (Amtout and Leonelli, 1995; Tang et al., 1995). The band gap energies for $ZnFe_2O_4/SiO_2$ composite coated with TiO_2 particles after annealing process varied from 3.13 eV to 3.25 eV.

Widening of the bandgap region may lead to various defects and discrete energy states. Therefore, it is important to study the radiative recombination transitions occurring in the prepared nanomaterial. In this regard, the fluorescence spectroscopy analysis of the obtained photocatalysts was performed and shown in Fig. 5.

The photoluminescent emission of the photocatalyst is a result of photoinduced electron-hole pairs recombination. The lower PL intensity indicates (i) inhibition of charge carriers recombination, therefore, the higher photocatalytic activity of $ZnFe_2O_4/SiO_2/TiO_2$_650_I and $ZnFe_2O_4/SiO_2/TiO_2$_650_II photocatalysts can be attributed to enhancing charge carriers' separation (Zhu et al., 1998). The PL emission spectra of $ZnFe_2O_4/SiO_2/TiO_2$ photocatalysts calcined at 400 °C and 650 °C has examined in the wavelength range of 350 to 700 nm. In the spectra, several emission regions can be distinguished. The emission band from 390 to 400 nm results from the photoexcited charge carriers recombination of TiO_2 (Mathew et al., 2012). The intensity of PL in this region is higher for pure TiO_2 and the sample $ZnFe_2O_4/SiO_2/TiO_2$_400 calcined at 400 °C than for sample $ZnFe_2O_4/SiO_2/TiO_2$_650_I annealed at 650 °C. The emission peaks at 420; 440 and 455 nm can be ascribed to a shallow-trap state near the absorption band edge, which results from the presence of oxygen vacancies (Zhu et al., 1998). The emission peak at 530 nm can be assigned to deep-trap states related to the presence of oxygen vacancies in the TiO_2 structure (Tehrani et al., 2012).

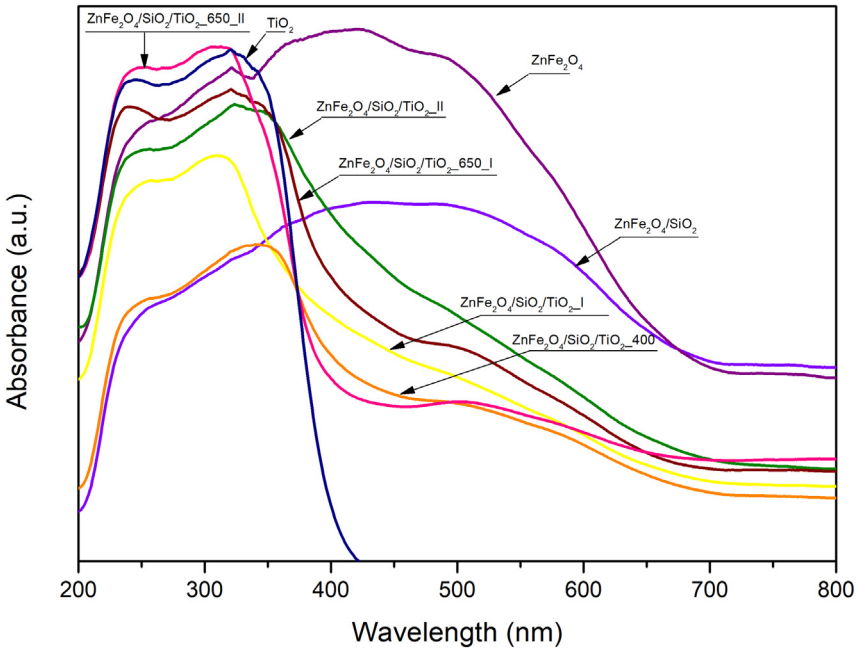

Fig. 4. Diffuse reflectance spectra of $ZnFe_2O_4$, $ZnFe_2O_4/SiO_2$, pure TiO_2 used as a reference, $ZnFe_2O_4/SiO_2/TiO_2$ without thermal treatment and $ZnFe_2O_4/SiO_2/TiO_2$ photocatalysts calcined at 400 °C and 650 °C.

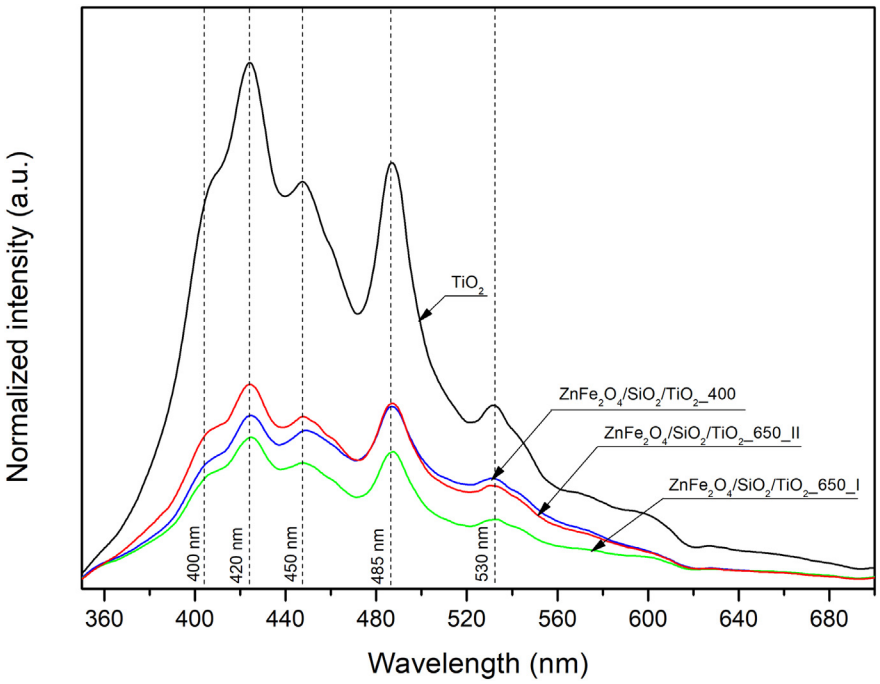

Fig. 5. Photoluminescence spectra of $ZnFe_2O_4/SiO_2/TiO_2$ photocatalysts at room temperature: (a) $ZnFe_2O_4/SiO_2/TiO_2$_650_II; (b) $ZnFe_2O_4/SiO_2/TiO_2$_400 and (c) $ZnFe_2O_4/SiO_2/TiO_2$_650_I.

3.2. Photolytic and photocatalytic degradation of etodolac in the presence of $ZnFe_2O_4/SiO_2/TiO_2$ nanocomposites

3.2.1. The effect of radiation range

The effective utilization of solar energy (UV–Vis) plays an important role in photocatalysis. Therefore, photolysis reaction and photocatalytic degradation of etodolac were performed under simulated solar light by using a 300 W Xenon lamp. The cut-off filters were applied to measure the photoactivity under UV light (optical filter UG transmitted light in the range of 250÷400 nm; max. 330 nm), and Vis light (optical filter transmitted light of wavelength >400 nm).

In order to study the effect of dark reaction of the magnetic photocatalyst, their components, and bare TiO_2 as the reference sample, the photodegradation analyses under UV–Vis irradiation proceeded. The adsorption-desorption equilibrium was established for 30 min in the absence of light. As shown in Fig. S3 in the Supporting materials, the adsorption ratio for the $ZnFe_2O_4/SiO_2/TiO_2$_II photocatalyst was equal to 13% after 30 min. Similarly, the etodolac adsorption on the surface of the magnetic core $ZnFe_2O_4$ amounted to 11%. For $ZnFe_2O_4/SiO_2$ particles with a developed specific surface, the adsorption ratio exceeded 30%. The reference sample of TiO_2 powder obtained an equivalent result.

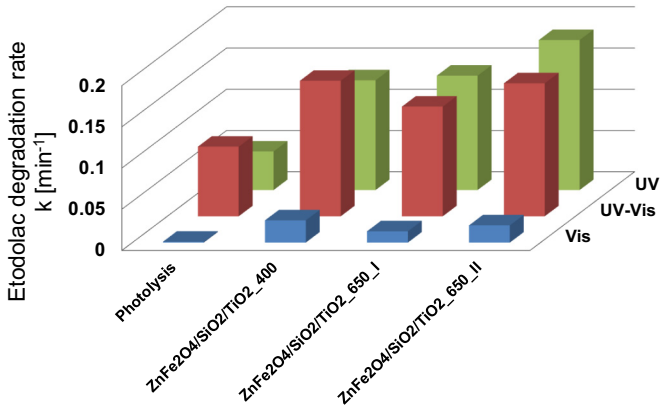

Fig. 6. The effect of irradiation range (Vis λ > 420 nm; UV 250 nm < λ < 400 nm; simulated solar light (UV–Vis) on photodegradation of etodolac.

As presented in Fig. 6, all the obtained photocatalysts promoted the effective photodegradation of etodolac.

The ability of light in photolysis to reduce etodolac concentration depended on the range of the light spectrum. There was no progress observed in etodolac photolytic degradation under Vis light irradiation. As shown in Fig. S4 in the Supporting materials, the extension of the photocatalytic process up to 60 min does not make a positive contribution into etodolac degradation under Vis light irradiation.

The efficiency of etodolac photolytic degradation after 30 min under UV light exceeded 60%, however, the highest degradation rate was observed under UV–Vis irradiation. Thus, it can be assumed that irradiation under a wide light range may reveal a synergetic effect on etodolac degradation efficiency. Compared with photolysis, the degradation of etodolac in the presence of $ZnFe_2O_4/SiO_2/TiO_2$_400 and $ZnFe_2O_4/SiO_2/TiO_2$_650_II photocatalysts was significantly improved under UV and visible light irradiation (>420 nm).

For the photocatalytic reaction in the presence of $ZnFe_2O_4/SiO_2/TiO_2$_650_II about 100% of etodolac was removed within 20 min of irradiation under UV and UV–Vis light (see in Fig. 7a). It is worth noting that the mineralization by $ZnFe_2O_4/SiO_2/TiO_2$ photocatalyst was markedly higher compared to the photolytic reaction, as shown in Fig. 7b. The highest TOC removal was observed under UV–Vis light for photocatalytic degradation in the presence of $ZnFe_2O_4/SiO_2/TiO_2$_650_II photocatalyst containing anatase phase with a small amount of rutile (3–4.5%).

3.2.2. The effect of initial pH on the photocatalytic performance

The initial pH of the aqueous phase is one of the most important parameters which affects photocatalytic activity. The UV–Vis spectroscopy was used to determine the pH effect on etodolac stability, as presented in Fig. 8. The UV–Vis spectrum of etodolac showed an absorption band with a maximum at the wavelength of about 220 nm and a shoulder of 270 nm. The results showed that there was no effect of pH on the absorption spectrum of etodolac.

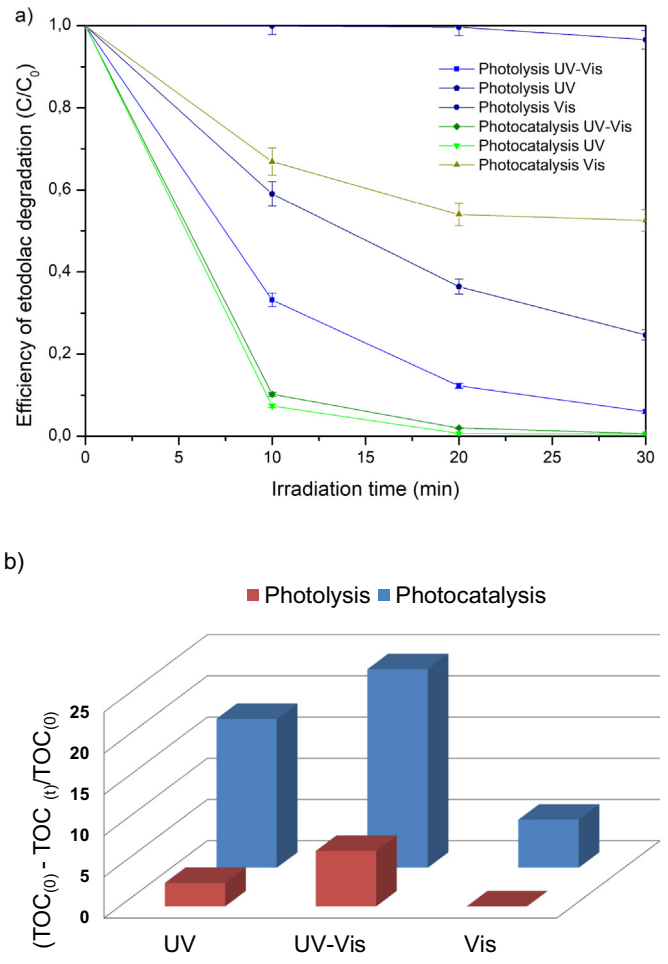

Fig. 7. The efficiency of etodolac degradation in photolysis and photocatalytic reaction under Vis, UV and UV–Vis light irradiation (a) and total organic carbon reduction (TOC) by photolysis and photocatalysis in the presence of Vis, UV and UV–Vis light (b). Experimental conditions: etodolac initial concentration $C_o = 0.5 \cdot 10^{-4}$ M, photocatalyst loading m = 0.05 g·dm^{-3}, 300 W xenon lamp.

The stability of etodolac in the dark reaction was analyzed at 20 °C at pH 4, 7, and 9. These pHs are usually considered environmentally relevant (Valenti et al., 2009). There was no degradation of etodolac observed after 1 h of mixing. The influence of initial pH in the range of 4 to 9 on the etodolac photocatalytic degradation was studied, and the results are presented in Fig. 9.

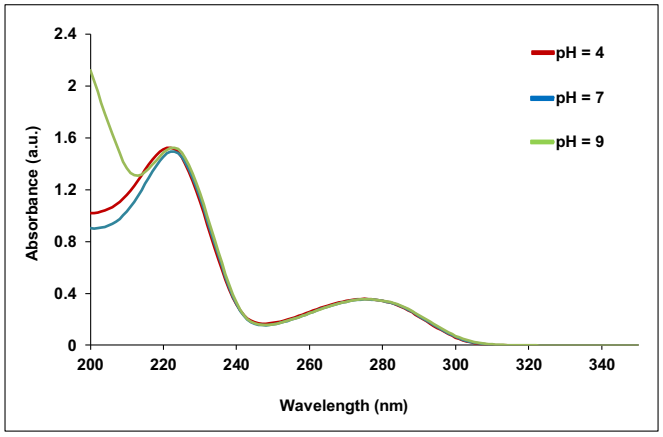

Fig. 8. UV–Vis spectra of etodolac at different pH values.

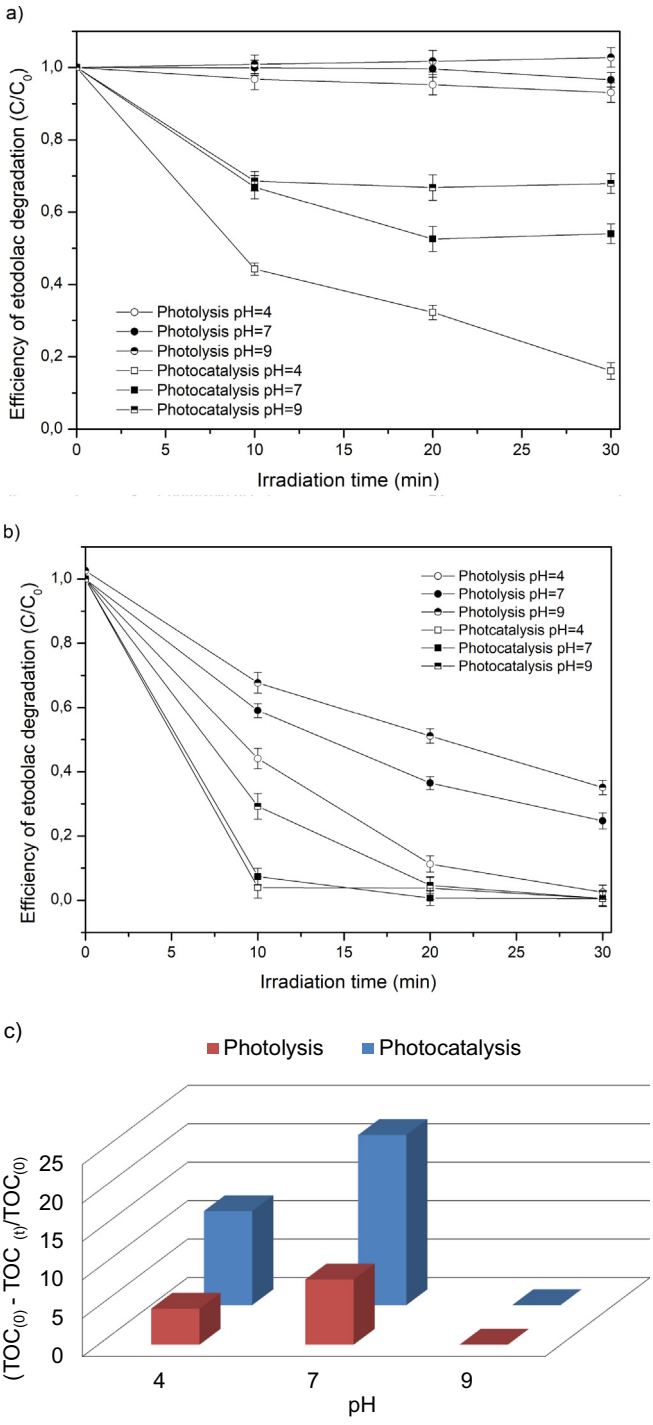

Fig. 9. The effect of initial pH on the etodolac removal under Vis light (a) under UV light (b) and the TOC removal fraction as a function of pH for $ZnFe_2O_4/SiO_2/TiO_2$_650_II under UV light irradiation (c).

It was observed that a pH above 4 and below 7 facilitated the etodolac removal. Under visible light, the highest efficiency of etodolac degradation was observed at pH = 4. After 30 min of irradiation, about 7% and 84% of etodolac were removed in photolytic and photocatalytic reactions, respectively (see in Fig. 9a).

The highest photodegradation of etodolac was noticed at a pH of 4 and 7 in the presence of UV light, as shown in Fig. 9b. The photolytic removal of etodolac was 58% at pH = 4 and 78% at a pH of 7 during 30 min of irradiation. At the same time, after 20 min of irradiation, the photocatalytic performance at pH = 4 was 97% and increased to 100% at

pH = 7. However, as the pH value further increased to 9, the photocatalytic activity decreased due to the quenching effect of carbonates under alkaline conditions. The presence of CO_3^{2-} and HCO_3^- presence results in adsorption and inorganic layer formation on the photocatalyst surface, and therefore hindering adsorption of other species (Farner Budarz et al., 2017; Guillard et al., 2005). Moreover, carbonate anions could act as a scavengers of the generated hydroxyl radicals, which reacts with the active species produced in the photocatalytic reaction and reduce the photocatalytic performance (Zhang et al., 2015). Scavenging of photogenerated hydroxyl radicals may especially explain almost full inhibition of TOC removal at alkaline conditions, as shown in Fig. 9c. Finally, at pH = 9 both etodolac and the surface of $ZnFe_2O_4/SiO_2/TiO_2$_650_II magnetic photocatalyst are expected to be negatively charged, which should promote their repulsion through electrostatic interactions.

Etodolac is a weakly acidic pharmaceutical agent having a pK_a of 4.65. Its solubility depends on the pH of the aqueous phase and increases significantly above the pK_a value. The pH of isoelectric point (pH_{IEP}) for $ZnFe_2O_4/SiO_2/TiO_2$_650_II was about 4.7, as shown in Fig. S5 in the Supporting materials. The photocatalyst surface was positively charged at pH < pH_{IEP} and negatively charged at pH > pH_{IEP}. At acidic conditions below pH_{IEP}, the photocatalyst was positively charged and was facilitated for the attraction of electron-rich aromatic nucleus or the oxygens of the etodolac molecule. The higher stability of suspension was noticed at pH above 6 and below 4. In this regard, the highest efficiency of etodolac removal was observed at pH above pKa value and below 7.

The most active in the reaction of etodolac degradation photocatalyst $ZnFe_2O_4/SiO_2/TiO_2$_650_II was selected for the reusability studies. In order to examine the photocatalytic effectiveness of the magnetic photocatalyst after its recovery, the six subsequent cycles were carried out, as can be seen in Fig. 10. At the end of each run of etodolac degradation, $ZnFe_2O_4/SiO_2/TiO_2$_650_II nanoparticles were separated from reaction slurry by an external magnetic field and then treated etodolac solution was discharged. Afterward, the separated photocatalyst was reused without any treatment. High efficiency of photocatalytic degradation was maintained after six subsequent cycles, without any loss in etodolac degradation and photomineralization. Mean TOC reduction TOC_0-TOC_t/TOC_0 for each cycle amounted to 0.62 ± 0.05.

3.3. Degradation mechanism and pathway

To verify the mechanism of photocatalytic activity the fluorescence spectra analysis of 3 mM terephthalic acid (TA) solution under UV–Vis was performed. A fluorescent product of TA photocatalytic reaction with ·OH is 2-hydroxyterephthalic acid (2-HTA), which emits fluorescence at 426 nm, as shown in Fig. S6 in the Supporting materials. There was no peak observed for the TA before irradiation indicating that fluorescence was linked only to the 2-HTA presence. The characteristic fluorescence of 2-HTA increased with the irradiation time, suggesting that the $ZnFe_2O_4/SiO_2/TiO_2$_650_II photocatalyst can produce ·OH under UV–Vis irradiation.

Furthermore, to provide insight into the mechanism of etodolac removal, oxidative species participating in the photocatalytic reaction have been investigated by reference experiments in the presence of scavengers. Photocatalytic activity of $ZnFe_2O_4/SiO_2/TiO_2$_650_II in reaction of etodolac degradation in the presence of tert-butanol (hydroxyl radicals (·OH) scavenger,), benzoquinone (superoxide radical anion ($\bullet O_2^-$) scavenger), ammonium oxalate (hole (h^+) scavenger) and silver nitrate (electron (e^-) scavenger) are presented in Fig. 11. The etodolac photocatalytic degradation determined without scavengers served as a reference sample.

The introduction of t-BuOH trapping the photogenerated hydroxyl radicals had little effect on the efficiency of etodolac degradation and its mineralization. The photocatalytic performance was significantly

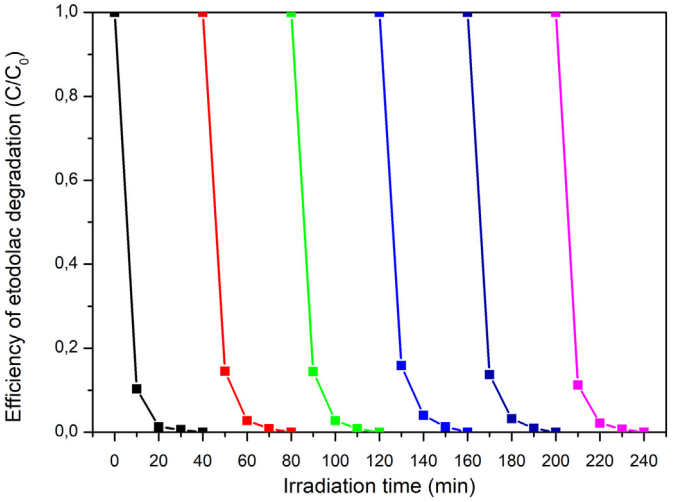

Fig. 10. The efficiency of etodolac degradation in the presence of $ZnFe_2O_4/SiO_2/TiO_2$_650_II photocatalyst measured in the six subsequent cycles of degradation.

suppressed in the presence of benzoquinone, indicating that $\bullet O_2^-$ plays an important role in photodegradation or competes with the potential active species involved in the degradation process. In the presence of ammonium oxalate, which was introduced as the scavenger of photogenerated holes (h^+), the photodegradation reaction was suppressed by 10%, suggesting that h^+ also played a role in the degradation of etodolac. The 2-times lower mineralization measured as TOC inhibition efficiency was observed for the photoreaction proceeded with the addition of $\cdot O_2^-$ scavenger and h^+ scavenger.

To further study the photocatalytic degradation mechanism, the HPLC/MS analyses of photooxidation and photodegradation products were performed.

The initial steps of etodolac photolysis in the presence of UV-A, UV-B or sunlight irradiation reported by Passananti et al. suggest the generation of two main photoproducts in the form of spiro (product **3**) and lactam (product **4**) compounds, respectively (Guzela et al., 2019). As presented in Fig. 12, the transformation of etodolac is initiated by reactive oxygen species attack on the C2-C3 bond of pyrrole ring in the excited molecule, which is also characteristic for the oxidation of indoles in other processes (Xu et al., 2019; McClay et al., 2005; Iesce et al., 2005). Obtained radical intermediate should further undergo series of spontaneous rearrangements to possibly give products **2**, **3** and **4**,

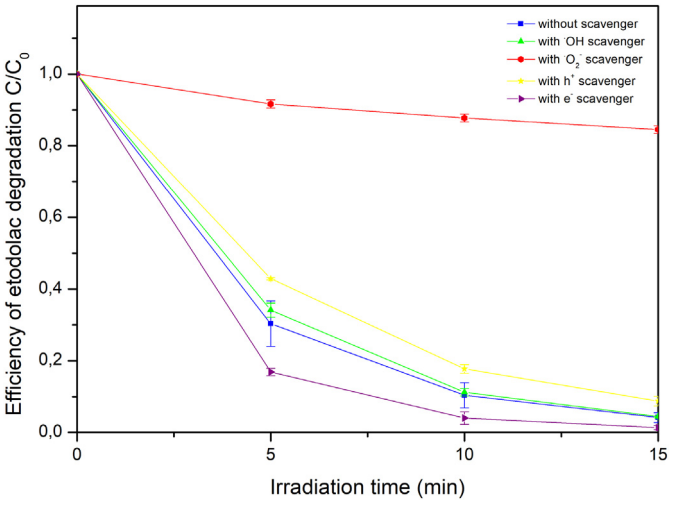

Fig. 11. Photocatalytic degradation of etodolac for $ZnFe_2O_4/SiO_2/TiO_2$_650_II photocatalyst in the presence of e^-, h^+, $\bullet O_2^-$, and •OH scavengers.

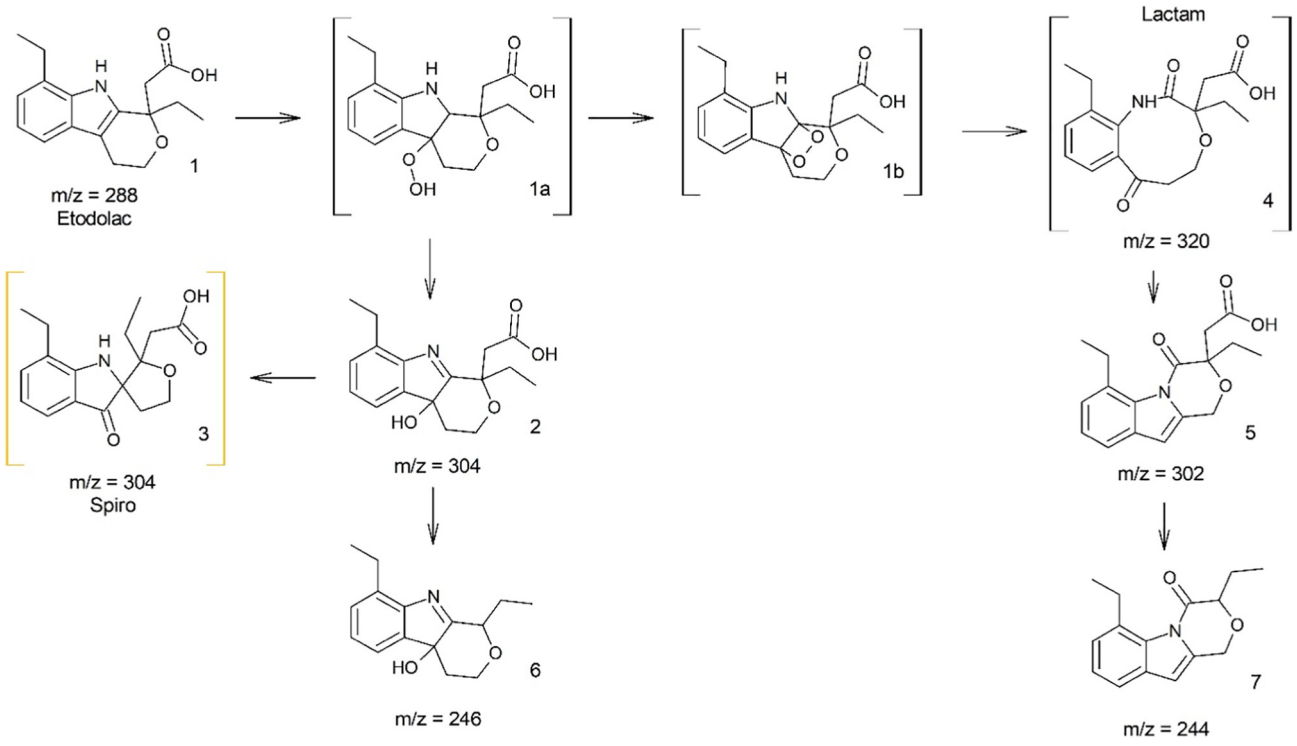

Fig. 12. The proposed mechanism of initial etodolac photodegradation under UV–Vis.

from which **3** and **4** were identified as main stable derivatives, with $m/z = 304$ and 320, respectively.

The compound with m/z = 304 was observed for both photolytic and photocatalytic processes. Moreover, in the presence of $ZnFe_2O_4/SiO_2/TiO_2$_650_II photocatalyst, an additional signal with $m/z = 302$ was found, which can be the product of compound **4** dehydration, marked as **5**. The analogical process was already observed by Afsah et al. in their study on the reactivity of dibenzo-azonines (Afsah et al., 2015), where compounds similar to lactam **4** underwent cyclodehydration under the Schmidt reaction conditions (NH_3/H^+). The formation of both possible byproducts during the photocatalytic process corresponds well with the observed role of $\bullet O_2^-$ species in the degradation of etodolac and suggested formation of hydroperoxide **1a** after initial oxygen addition to the double bond of the pyrrole ring of etodolac (compound **1**). According to literature, a spiro derivative 3 with $m/z = 304$ should absorb UV light with a maxima at 225 nm and 255 nm (Passananti et al., 2015). In this study, no similar compound was observed. Instead, the formation of a derivative 2 with three maxima at 215 nm, 256 nm, and 292 nm was detected. Since compound **2** is presented as a parent for a spiro, it is suggested that it was mainly observed as m/z = 304 compounds. Stabilization of a structure **2** occurred due to a lack of mineral acid catalyst, which was required to perform the described transformation in a quantitative yield, as described by Mateo and co-workers (Mateo et al., 1996). Therefore, the formation of compound **2** as the main oxidation product of photocatalytic degradation was observed.

Both compounds **2** and **5** can later undergo -CH_2-COOH detachment to form compounds with m/z = 246 and m/z = 244, derivatives **6** and **7**, respectively. Product **6** was observed on the MS spectrum mainly during the photocatalytic process, while the formation of compound **7** was found mostly during the photolysis of ETD in acidic conditions. The transformation was based on a hydroxyl attack on α-carbon, relative to carboxyl moiety, which was also found to be promoted in the presence of ·OH radicals in citric acid (CA) oxidation (Zeldes and Livingston, 1971; Meichtry et al., 2011).

Further, compounds **6** and **7** can undergo breaking of hydropyrane ring. This results in the formation of 7-ethyl-tryptophol derivative (structure **8** in Fig. 13) or other indolic compounds, together with corresponding ketones as byproducts.

Indeed mainly at acidic conditions, spontaneous formation of a compound with board single absorption maximum at 274 nm was observed, which corresponds to 2-butanone (Lee et al., 1988; Schütze and

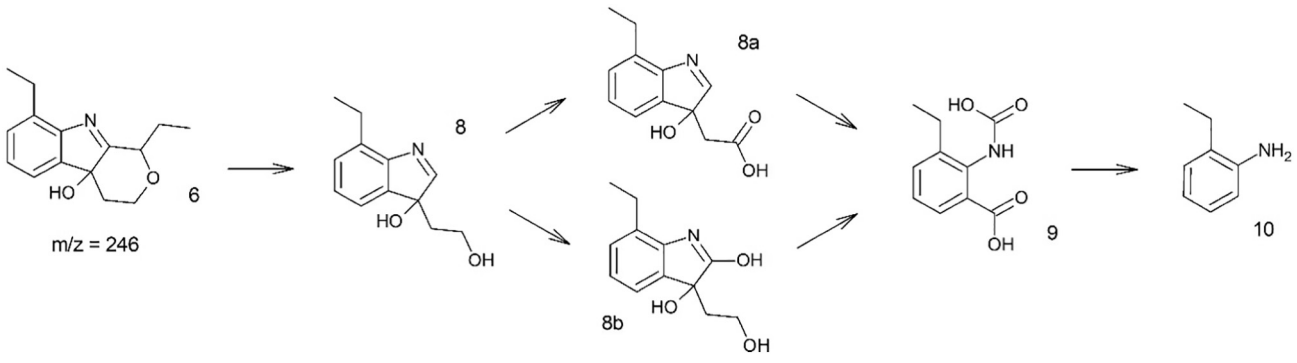

Fig. 13. The suggested further steps of etodolac degradation under UV–Vis.

Herrmann, 2004). Its formation was additionally promoted under visible light irradiation, what's shown in Fig. S7 in the Supporting materials, suggesting that similar transformation could be crucial for increased TOC removal under the UV–Vis spectrum, rather than UV only.

The presence of 2-butanone was mainly found in photolytic degradation at pH = 4, while during the photocatalytic process the compound quickly disappeared, suggesting its further efficient mineralization. It can be reasoned that photocatalyst presence can promote similar process to photolysis but with more efficiency, either through formation of reactive oxygen species ($\bullet O_2^-$, •OH) as well as positively charged states of TiO_2 by h^+ trapping on the surface or because of Lewis-acidic active sites, that are characteristic for anatase structure (Pérez-López et al., 2018; Martra, 2000). The involvement of ROS and photogenerated holes in the mechanism of etodolac degradation was confirmed, since the significant effect of h^+ and $\bullet O_2^-$ scavenging on TOC removal was observed.

Furthermore, the Mott-Schottky analysis was performed to determine the location of flat band energy (E_{fb}) by measuring the space charge region capacitance (C_{sc}) at electrode/electrolyte interface, according to Eq. (1).

$$C_{sc} = -\frac{1}{Z''\omega} \quad (1)$$

C_{sc} – capacitance of the space charge region, Z'' – imaginary impedance, ω – angular frequency.

Model Mott-Schottky plots of the $ZnFe_2O_4/SiO_2/TiO_2$_650_II sample are presented in Fig. S8 in the Supporting materials. The capacitance of the space charge region was calculated for three different frequencies, resulting in three different values of E_{fb}. The differences in Mott-Schottky plots for various data series are observed due to the electrode porosity and increasing faradaic current influence on the current distribution at low-frequencies (Scribner, 1990).

The Mott-Schottky plots indicated that the analyzed photocatalyst acts as the p-type semiconductor. The flat band potential of photocatalyst was estimated at 1.7 V vs. Ag/AgCl (0.1 M KCl), therefore for the p-type material, the valence band edge is expected to be placed slightly lower to its flat band potential (Babu et al., 2014). The position of conductive band edge was estimated as the difference between the flat band edge position (1.7 V vs. Ag/AgCl (0.1 M KCl), equal to 1.988 V vs. NHE) and the band gap value E_g (3.25 eV) and amounted −1.212 V vs. NHE. Fig. 14 shows the proposed value of the conductive band edge (C_B) and the respective position of the flat band (E_F) with corresponding energy of valence band edge (V_B). According to the estimated results of C_B and V_B position, the examined photocatalyst can efficiently oxidize H_2O into oxygen and reduce oxygen particles into superoxide radicals. The presented results correspond with the photocatalytic analysis conducted in the presence of reactive oxygen species scavengers, where the photocatalytic activity of $ZnFe_2O_4/SiO_2/TiO_2$_650_II photocatalyst was significantly suppressed in the presence of $\bullet O_2^-$ scavenger.

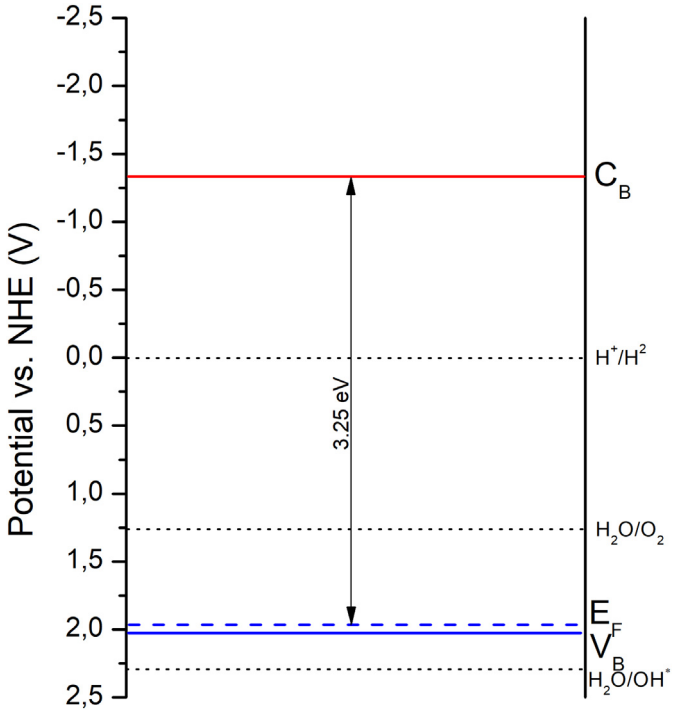

Fig. 14. Schematic representation of the energy positions of the conduction band (C_B) and flat band energy (E_F) with corresponding valence band (V_B) of $ZnFe_2O_4/SiO_2/TiO_2$_650_II photocatalyst.

Although TiO_2 is widely considered to be an n-type semiconductor, p-type semiconductivity of TiO_2 was already reported (Nowotny et al., 2010; Conrado et al., 2013). Acceptor dopants, such as cations with a lower valence than Ti^{4+}, can act as acceptors of electrons and shift the n-type to p-type transition. P-type behavior of TiO_2-based photocatalysts may results from the formation of titanium vacancies (acceptor-type defects). Kaariainen et al. obtained p-n junction in TiO_2 between p-type anatase and n-type rutile. The polycrystalline materials revealed enhanced photocatalytic performance compared to the n-type TiO_2, which indicates that superior photoactivity results from the formation of p-n heterojunction (Conrado et al., 2013).

4. Conclusions

In summary, the $TiO_2/SiO_2/ZnFe_2O_4$ magnetic photocatalysts were synthesized successfully and used for the first time in the photodegradation of etodolac. This study provides new insight into the application of heterogeneous photocatalysis, where pollutants are chemically oxidized by nonselective free radical species, for degradation of xenobiotics under simulated solar light.

The significantly enhancement of photocatalytic activity can be attributed to the p-n junction in TiO_2 of the $TiO_2/SiO_2/ZnFe_2O_4$_650_II composite material. The trapping experiments revealed that h^+, $\bullet O_2^-$, and •OH were ROS involved in ETD photocatalytic degradation. The PL spectra analysis showed the lower intensity for $ZnFe_2O_4/SiO_2/TiO_2$ magnetic photocatalysts than for pure TiO_2_400, which indicates lower electron-hole recombination rate and higher photocatalytic activity. The photocatalytic tests in the present of ROS scavengers as well as the Mott-Schottky analysis confirmed that the studied magnetic photocatalyst can efficiently oxidize H_2O into oxygen and reduce oxygen particles into superoxide radicals.

The effect of irradiation range on the ability to reduce etodolac concentration in photolysis and photocatalytic degradation was confirmed. There was no progress observed in etodolac photolytic degradation under Vis light irradiation.

The highest efficiency of etodolac removal was observed at pH above the pKa value of etodolac and below pH = 7 under UV and UV–Vis light. Compared with photolysis, the degradation of etodolac in the presence of $ZnFe_2O_4/SiO_2/TiO_2$ photocatalysts was markedly improved under UV and visible light. After 20 min of irradiation, about 100% of etodolac was decomposed. Based on HPLC/DAD and HPLC/MS analysis six intermediates were determined both in photolysis and photocatalytic reaction and the degradation pathway of photodegradation was proposed.

Funding

The research was financially supported by Polish National Science Centre (Grant No. NCN 2018/30/E/ST5/00845).

CRediT authorship contribution statement

Eryka Mrotek: Formal analysis, Resources, Investigation, Writing - review & editing.**Szymon Dudziak:**Formal analysis, Investigation, Writing - review & editing.**Izabela Malinowska:**Resources, Investigation, Writing - review & editing.**Daniel Pelczarski:**Investigation.**Zuzanna Ryżyńska:**Investigation.**Anna Zielińska-Jurek:**Conceptualization, Methodology, Resources, Writing - original draft, Writing - review & editing, Supervision, Project administration, Funding acquisition.

Declaration of competing interest

The authors declare that they have no known competing financial interests or personal relationships that could have appeared to influence the work reported in this paper.

Acknowledgments

This research was financially supported by the Polish National Science Centre, grant no. NCN 2016/23/D/ST5/01021 and Polish Ministry of Science and Higher Education grant no. 0525/E-359/STYP/13/2018 Scholarships for outstanding young scientists. We also acknowledge Piotr Jan Jurek for graphical abstract design and drawing.

Appendix A. Supplementary data

Supplementary data to this article can be found online at https://doi.org/10.1016/j.scitotenv.2020.138167.

References

Abdel-Wahab, A.M., Al-Shirbini, A.S., Mohamed, O., Nasr, O., 2017. Journal of Photochemistry and Photobiology A:Chemistry 347, 186–198.
Afsah, E.M., Fadda, A.A., Bondock, S., Hammouda, M.M., 2015. Zeitschrift Fur Naturforsch, Sect. B Journal of Chemical Sciences 70, 385–391.
Amtout, A., Leonelli, R., 1995. Phys. Rev. B 51, 6842.
Babu, R., Kelkar, S., Kashid, V., Achary, S., Salunke, H., Gupta, N., 2014. RSC Adv. 4, 33435–33445.
Brocks, D.R., Jamali, F., 1994. Etodolac clinical pharmacokinetics. Clin. Pharmacokinet. 26, 259–274.
Conrado, J., Fresno, F., Hernandez-Alonso, M., Portela, R., 2013. Green Energy and Technology. Springer.
Farner Budarz, J., Turolla, A., Piasecki, A.F., Bottero, J.Y., Antonelli, M., Wiesner, M.R., 2017. Langmuir 33, 2770.
Folli, A., Pochard, I., Nonat, A., Jakobsen, U.H., Shepherd, A.M., Macphee, D.E., 2010. J. Am. Ceram. Soc. 93, 3360–3369.
Gadade, D., Pekamwar, S., LahotI, S.R., PatnI, S.D., Sarode, M.C., 2017. Marmara Pharmaceutical Journal 21, 78–88.
Gambarotti, C., Melone, L., Punta, C., 2012. Semiconductors in Organic Photosynthesis, Artificial Photosynthesis February 24th.
Guillard, C., Puzenat, E., Lachheb, H., Houas, A., Herrmann, J.-M., 2005. International Journal of Photoenergy 7, 1.
Guzela, E.Y., Cevika, F., Daglioglu, N., 2019. Human and Ecological Risk Assessment: An International Journal 25, 1980–1995.
Hoshina, K., Horiyama, S., Matsunaga, H., Haginaka, J., 2011. J. Pharm. Biomed. Anal. 55, 916–922.
Howard, P.H., Muir, D.C.G., 2011. Environmental Science & Technology 45, 6938–6946.
Iesce, M., Cermola, F., Temussi, F., 2005. Curr. Org. Chem. 9, 109–139.
Kanakaraju, D., Glass, B.D., Oelgemöller, M., 2018. J. Environ. Manag. 219, 189–207.
Kurian, J., Mathew, M.J., 2018. J. Magn. Magn. Mater. 451, 121.
Lee, Y.J., Padula, J., Lee, H., 1988. J. Pharm. Sci. 60, 1193–1196.
Lee, S.A., Choo, K.H., Lee, C.H., Lee, H.I., Hyeon, T., Choi, W., Kwon, H.H., 2001. Ind. Eng. Chem. Res. 40, 1712–1719.
Lee, J.S., Cha, J.M., Yoon, H.Y., Lee, J.K., Kim, Y.K., 2015. Sci. Rep. 5.
Liu, Y., Tourbin, M., Lachaize, S., Guiraud, P., 2013. Chemosphere 92, 681–687.
Mansour, S.A., 2019. Ceram. Int. 45, 2893–2898.
Martra, G., 2000. Applied Catalysis A. General 200, 275–285.
Mascolo, M.C., Pei, Y., Ring, T.A., 2013. Materials 6, 5549.
Mateo, C.A., Urrutia, A., Rodríguez, J.G., Fonseca, I., Cano, F.H., 1996. J. Org. Chem. 61, 810–812.
Mathew, S., Kumar Prasad, A., Benoy, T., 2012. J. Fluoresc. 22, 1563–1569.
McClay, K., Boss, C., Keresztes, I., Steffan, R.J., 2005. Appl. Environ. Microbiol. 71, 5476–5483.
Meichtry, J.M., Quici, N., Mailhot, G., Litter, M.I., 2011. Applied Catalysis B Environmental 102, 555–562.
Meng, X., Zhuang, Y., Tang, H., Lu, C., 2018. J. Alloys Compd. 761, 15–23.
Mishra, Priti, Patnaik, Sulagna, Parida, Kulamani, 2019. Catalysis Science & Technology https://doi.org/10.1039/C8CY02462F.
Mozaffari, M., Eghbali Arani, M., Amighian, J., 2010. J. Magn. Magn. Mater. 322, 3240.
Nowotny, M., Bogdanoff, P., Dittrich, T., Fiechter, S., Fujishima, A., Tributsch, H., 2010. Mater. Lett. 64, 928–930.
Ohno, T., Sarukawa, K., Tokieda, K., Matsumura, M.J., 2001. J. Catal. 203, 82–86.
Ohtani, B., 2010. J Photochem Photobiol C: Photochem Rev 11, 157–178.
Ohtani, B., Ogawa, Y., Nishimoto, S., 1997. J. Phys. Chem. B 5647, 3746–3752.
Passananti, M., Lavorgna, M., Iesce, M.R., DellaGreca, M., Brigante, M., Criscuolo, E., Cermola, F., Isidori, M., 2015. Sci. Total Environ. 518–519, 258–265.
Pérez-López, G., Ramírez-López, R., Viveros, T., 2018. Catal. Today 305, 182–191.
Porter, J.F., Li, Y.G., Chan, C.K., 1995. J. Mater. Sci. 34, 1523.
Saxena, D., Damale, S., Datar, A., 2016. Int J Pharm Pharm Sci 8, 127–135.
Schütze, M., Herrmann, H., 2004. Phys. Chem. Chem. Phys. 965–971.
Scribner, L.L., 1990. The Measurement and Correction of Electrolyte Resistance in Electrochemical Tests. ASTM International.
Shanmugavani, A., Kalai Selvan, R., Layek, S., Sanjeeviraja, C., 2014. J. Magn. Magn. Mater. 354, 363.
Tang, H., Levy, F., Berger, H., Schmid, P.E., 1995. Phys. Rev. B 52, 7771.
Tehrani, F.S., Daadmehr, V., Rezakhani, A.T., Akbarnejad, R.H., Gholipour, S., 2012. J. Supercond. Nov. Magn. 25, 2443–2455.
Teimouri, M., Husain, S.W., Saber-Tehrani, M., Aberoomand-Azar, P., 2019. Sep. Sci. Technol. 54.
Temussi, F., Cermola, F., DellaGreca, M., Iesce, M.R., Passananti, P., Previtera, L., Zarrelli, A., 2011. J. Pharm. Biomed. Anal. 56, 678–683.
Tomita, K., Kawano, M., 1993. Rep. Fac. Sci. Kagoshima Univ 26, 1–16.
Valenti, T.W., Perez-Hurtado, P., Chambliss, C.K., Brooks, B.W., 2009. Environ. Toxicol. Chem. 28, 2685–2694.
Watanabe, H., Tamura, I., Abe, R., Takanobu, H., Nakamura, A., Suzuki, T., Hirose, A., Nishimura, T., Tatarazako, N., 2016. Environ. Toxicol. Chem. 35, 996–1006.
Xu, J., Liang, L., Zheng, H., Chi, Y.R., Tong, R., 2019. Nat. Commun. 10, 1–11. https://doi.org/10.1038/s41467-019-12768-4.
Yao, C., Zeng, Q., Goya, G.F., Torres, T., Liu, J., Wu, H., Ge, M., Zeng, Y., Wang, Y., Jiang, J.Z., 2007. J. Phys. Chem. C 111, 12274.
Zeldes, H., Livingston, R., 1971. J. Am. Chem. Soc. 93, 1082–1085.
Zhang, Q., Gao, L., Guo, J., 2000. Appl. Catal. B Environ. 26, 207.
Zhang, G., He, X., Nadagouda, M.N., O'Shea, K.E., Dionysiou, D.D., 2015. Water Res. 73, 353.
Zhu, Y., Ding, C., Ma, G., Du, Z., 1998. J. Solid State Chem. 139, 124–127.
Zielińska-Jurek, A., Bielan, Z., Dudziak, S., Wolak, I., Sobczak, Z., Klimczuk, T., Nowaczyk, G., Hupka, J., 2017a. Catalysts 7, 360.
Zielińska-Jurek, A., Bielan, Z., Wysocka, I., Strychalska, J., Janczarek, M., Klimczuk, T., 2017b. J. Environ. Manag. 195, 157–165.